Article:
Al-Shammari, AA, Kissane, RWP, Holbeck, S et al. (5 more authors) (2019) Integrated method for quantitative morphometry and oxygen transport modelling in striated muscle. Journal of Applied Physiology, 126 (3). pp. 544-557. ISSN 8750-7587

https://doi.org/10.1152/japplphysiol.00170.2018

An integrated method for quantitative morphometry and oxygen transport modelling in striated muscle

*Abdullah A. Al-Shammari[1, 2, *], Roger W.P. Kissane[3, *], Simon Holbek[4, *], Abigail L. Mackey[5,6], Thomas R. Andersen[7], Eamonn A. Gaffney[1], Michael Kjaer[5,8], and Stuart Egginton[3]*

[1] Wolfson Centre for Mathematical Biology, Mathematical Institute, University of Oxford, Oxford, OX2 6GG, United Kingdom.
[2] Department of Mathematics, Faculty of Sciences, Kuwait University, P.O. Box 5969, Khaldiya 13060, Kuwait.
[3] School of Biomedical Sciences, Faculty of Biological Sciences, University of Leeds, Leeds LS2 9JT, United Kingdom.
[4] DTect, Copenhagen, Denmark
[5] Institute of Sports Medicine Copenhagen, Department of Orthopaedic Surgery M, Bispebjerg Hospital, Copenhagen, Denmark
[6] Center for Healthy Aging, Department of Biomedical Sciences, Faculty of Health and Medical Sciences, University of Copenhagen, Copenhagen, Denmark
[7] Copenhagen Centre for Team Sport and Health, Department of Nutrition, Exercise and Sports, University of Copenhagen, Copenhagen, Denmark,
[8] Center for Healthy Aging, Faculty of Health and Medical Sciences, University of Copenhagen, Copenhagen, Denmark.
[*] *To be considered equal in contribution and joint first authorship*

Author contribution: The project was formulated by SE and EAG, AAS and EAG established the code for oxygen transport modelling with input from SE. SH developed the code and pipeline for DTect, assisted by RWPK and TRA, who additionally optimised staining protocol for input into the DTect packages. RWPK completed all animal work, while ALM and MK conducted all human experiments and tissue collection. RWPK completed tissue processing, analysis and interpretation of data with SE. The manuscript draft was formulated by RWPK, AAS and SE, and the final draft approved by all authors.

Running Title: Realistic oxygen modelling in striated muscle

Corresponding Author: Professor Stuart Egginton. School of Biomedical Sciences, Faculty of Biological Sciences, University of Leeds, Leeds LS2 9JT, United Kingdom. Email: s.egginton@leeds.ac.uk

Abstract

Identifying structural limitations in O_2 transport is primarily restricted by current methods employed to characterise the nature of physiological remodelling. Inadequate resolution or breadth of available data has impaired development of routine diagnostic protocols and effective therapeutic strategies. Understanding O_2 transport within striated muscle faces major challenges, most notably in quantifying how well individual fibres are supplied by the microcirculation, which has necessitated exploring tissue O_2 supply using theoretical modelling of diffusive exchange. Having identified capillary domains as a suitable model for the description of local O_2 supply, and requiring less computation than numerically calculating the trapping regions that are supplied by each capillary *via* biophysical transport models, we sought to design a high throughput method for histological analysis. We present an integrated package that identifies optimal protocols for identification of important input elements, processing of digitised images with semi-automated routines, and incorporation of these data into a mathematical modelling framework with computed output visualised as the tissue partial pressure of O_2 (PO_2) distribution across a biopsy sample. Worked examples are provided using muscle samples from experiments involving rats and humans.

Key Words: Image Analysis, Mathematical Modelling, Skeletal Muscle, Fibre Type, Capillary Supply, DTect

New & Noteworthy: Progress in quantitative morphometry and analytical modelling have tended to develop independently. Real diagnostic power lies in harnessing both disciplines within one user-friendly package. We present a semi-automated, high-throughput tool for determining muscle phenotype from biopsy material, which also provides anatomically relevant input to quantify tissue oxygenation, in a coherent package not previously available to non-specialist investigators.

Introduction

Striated muscle is characteristically plastic, with the capacity to dynamically remodel in response to varying physiological, pharmacological and pathological stimuli. Microvascular remodelling (e.g. angiogenesis) in striated muscle has been identified as a highly coordinated physiological process (16), and being able to effectively explore the functional importance of targeted interventions or the consequential effect of pathology on microvascular O_2 transport would be a valuable resource for both basic science and translational investigations (46). In a muscle with uniform phenotype, such as cardiac muscle, this presents a relatively straightforward problem that may be solved by approximating a localised supply location (capillaries) and homogenous O_2 demand (fibre MO_2) in modelling the outcome (2, 26, 27). In most skeletal muscles, however, it is necessary to accommodate varying fibre type, fibre size and geometry, and microvascular distribution, in order to quantify the relationship between local supply and demand.

Analytical solutions for peripheral oxygen transport have been dominated by derivatives of the Krogh oxygen cylinder approach, despite involving a number of unrealistic assumptions (30) and lack of space-filling capability (19). Krogh postulated a model where each capillary within a muscle ran parallel with muscle fibres and supplied O_2 in a radial fashion, the area encompassed within a tissue cylinder defining the functional supply area for an individual capillary (31). This model relied on a variety of assumptions, for instance; that O_2 consumption was uniform across fibres, that capillaries were parallel and equally spaced, and that the average tissue partial pressure of O_2 (PO_2) equalled that of the average capillary PO_2 at the capillary wall (28). The use of such supply regions is clearly an unrealistic system for physiological O_2 delivery, given the inherent difficulty in close packing of cylinders (*i.e.* circles when represented as 2D tissue sections). This would indicate there are areas where no O_2 will diffuse (anoxic regions), and instances of overlapping supply areas that involve intercapillary interactions and excess O_2 delivery (30). Excluded regions of tissue O_2 supply within Krogh's cylinder method led to the testing of tessellating (space filling) polygons to remove these voids, with the capillary domain area developed as a useful quantitative index of capillary supply. Capillary domains describe the area of tissue supplied by an individual

capillary that incorporates tissue closest to its centroid than any other, with the domain boundary placed equidistant to the nearest capillaries. This tessellation of domains within a tissue cross section allows the functional relevance associated with the capillaries' spatial distribution to be analysed, within both homogeneous and heterogeneous tissue (20, 26). The distribution of domain areas also allows quantification of capillary heterogeneity, and the functional consequence of different fibre size to be incorporated into the analysis of local capillary supply (19).

The utility of capillary domains to represent O_2 flux fields has been explored using striated muscle with uniform O_2 uptake (cardiac tissue) (26), and tissue with asymmetrical capillary supply and heterogeneous O_2 demand (4), and compared with the more biophysically precise trapping regions (a numerical solution for the region supplied with O_2 by each capillary determined *via* the transport equations overlying the geometry generated from histological images) (4). Comparative simulations of capillary domains and trapping regions have been shown to be highly correlated in muscles with both uniform O_2 uptake, and in those with moderately heterogeneous demand (4). The dissociation between capillary domains and trapping regions only becomes apparent around abnormally large fibres, regions of tissue with unusually heterogeneous oxidative capacities, and in instances of significant capillary rarefaction (1, 4).

Structural changes in muscle are most commonly analysed using immuno/histochemical staining and laborious manual image processing techniques. Image-based modelling relies on unambiguous identification of discrete objects, processing of the image to allow their classification, and extracting pertinent details to define model parameters. Current quantification of anatomical composition from tissue sections predominantly utilise global indices of fibre composition and capillary supply, due to the time-consuming manner of acquiring finer scale morphometric indices, and the computational difficulty in modelling of O_2 transport. Standard operating procedures have been devised to allow unbiased and reproducible morphometric analysis (12, 18), with attempts to produce semi-automated (39) and fully automated analyses (34, 36, 43) for global morphometric indices. In principle, algorithms reduce operator bias to a minimum (reproducibility from

independent runs with fully automatic algorithms are close to 100%) and all fibres in an image can be classified much more quickly than traditional, manual approaches. This does, however, rely on unambiguous staining profiles (e.g. fibre boundaries must be detectable with an algorithm that produces a realistic outline, and individual fibres assigned to a specific phenotype), which is rarely achievable. Consequently, no current method provides the necessary flexibility for both delineating fibres at adequate resolution, nor associating individual capillaries with neighbouring fibres. The availability of such an intricate anatomical description in digitised form is essential if mathematical and computational models of O_2 transport, which require such detail, are to objectively explore the functional and structural relationship between microvascular supply and tissue demand during muscle remodelling (1, 4).

Therefore, the aim of this study has been to provide an integrative method for muscle biopsy analysis that provides a more comprehensive analytical approach than currently available. This necessitated developing a semi-automated image processing data pipeline feeding into a mathematical modelling framework for computing oxygen supply and demand, with improved throughput, whilst maintaining interactive capabilities for non-standard applications. Worked examples are provided using muscle samples from experiments involving rats (metabolic heterogeneity) and humans (leg immobilisation).

Material and methods

Animal sampling was conducted in accordance with UK Home Office guidelines, in accordance with the 1986 Animal (Scientific Procedures) Act. Rats were culled by Schedule 1 methods (concussion to the brain and cervical dislocation); the *m. tibialis anterior* (TA) was carefully removed, trimmed of distal tendons, the mid-portion coated with OCT on cork discs, snap frozen in isopentane cooled in liquid nitrogen, and stored at -80°C for later analysis.

All human participants gave written informed consent to be included in the study, which conformed to the standards set by the Declaration of Helsinki, and in accordance with local ethics

committee approval. We utilised a unilateral limb immobilisation cast to mimic bed-rest for two weeks, to investigate the effect on muscle phenotype and oxygen delivery kinetics (9, 40). Four healthy untrained males (age 22 ± 2 years, BMI 22.6 ± 2.2) were recruited to take part in this study. Two weeks unilateral lower limb immobilisation was performed using a lightweight fibre cast running from the malleoli to below the groin, with the knee positioned flexed and held at 50°. Participants were instructed to use crutches throughout the two-week casting. Samples from *m. vastus lateralis* (VL) were taken using a 5mm Bergström needle with suction. Samples were snap frozen in liquid nitrogen, and stored at -80℃ for later analysis.

Immunohistochemistry

Muscle samples were warmed to -20℃ for cryosectioning, serial sections cut at 10µm, and fixed to polysine adhesion slides (VWR International). Slides were stored at -20℃ until staining.

Fibre type composition and capillary location

Monoclonal-myosin heavy chain (MHC) antibodies were used to simultaneously label two of the three major fibre types; BA-D5 (1:1000 dilution) for Type I fibres (slow MHC) labelled with Alexa Fluor 555 Goat Anti-Mouse IgG (1:1000 dilution) (Life Technology, A21422) and SC-71 (1:500 dilution) for Type IIa (fast oxidative, glycolytic) labelled with Alexa Fluor 488 Rabbit Anti-Mouse IgG (1:1000 dilution) (Life Technology, A11059), with the remaining unstained fibres validated to be Type IIb/x. Fibre boundaries were identified using a fluorescent probe to the extracellular matrix protein, laminin (Sigma, L9393). Finally, capillaries were labelled with a carbohydrate-binding protein (lectin) specific to the species of interest: for rodent endothelial cells *Griffonia simplicifolia* lectin I (GSL I, Vector Labs, FL-1101; 1:250 dilution) and human endothelial cells *Ulex europaeus* agglutinin I (UEA I, Vector Labs, FL-1061; 1:250 dilution). This combination of markers provided reproducible differentiation of the three main fibre types and their boundary localization (Fig. 1A), allowing fibre-specific interaction with individual capillaries to be quantified (29, 37), in a protocol shown to be robust for both rodent and human samples (5, 29, 37). Images were taken using a Q Imaging MicroPublisher 5.0 RTV camera on a Nikon Eclipse E600 microscope, and taken at x20

magnification (440x330 μm^2, for rat TA) or x10 magnification (866x649 μm^2, for human VL) with a 2 second exposure across all three fluorescent channels.

Fibre type segmentation

A further development of the stand-alone graphical user interface, DTect, was coded in MATLAB (The MathWorks, Inc., Cambridge, UK) for semi-automatic fibre segmentation (37). Step I detects fibre borders based on an immunostained basal lamina image, and offers the user an option to edit the image (boost indistinct and remove artefact lamina segments) to improve delineation accuracy (Fig. 1B). The extent of manual intervention becomes a balance between threshold level and noise, but allows analysis with variable quality of staining. Step II is automated classification into different fibre types based on colour space of enclosed pixels and defined size range (Fig. 1A), but with the opportunity to correct classification of individual fibres to accommodate problems with sample preparation or age that may give rise to indistinct threshold boundaries. An output file with morphometric statistics grouped according to fibre type is produced at this point, with the option to proceed with further analysis. In step III capillary locations are manually marked on the image, based on vessel centre of gravity, and their position linked with adjacent fibres (Fig. 1C). Global indices of muscle capillary supply are then generated. Step IV generates an output file containing capillary and fibre border coordinates, with fibre type annotation, and is used as input for tissue oxygen tension computations (PO_2 distributions, see below).

Muscle fibre boundary identification

The goal is to create a binary image of the basal lamina where noise is filtered and a centerline skeleton preserved. An RGB image file (.jpg, .png, or .tif options available) from the immuno/histochemical method above is imported together with a record of the scaling factor (i.e. the pixel length in millimetres). In this study, blue fluorescence was used for lamina coding and a default threshold value used to create a binary image, with the aim of segmenting out the lamina in the image; further user refinement of the threshold value is possible to improve segmentation accuracy, or to accommodate pathological thickening. The actual value of the threshold adopted is

less important that the qualitative performance it allows, and the user readily evaluates this. Subsequently, all isolated pixels are cleared from the image i.e. treated as non-lamina segments, and a bridging operation, which ensures that gaps of one pixel size between unconnected pixels are treated as continuous lamina segments if they have two nonzero neighbours that are not connected. A morphological opening algorithm was applied to the image that filled all holes of single pixel size, and finally a closing algorithm was performed to shrink the binary image into a lamina skeleton of one pixel width, producing a connected line halfway between the inner and the outer lamina boundaries. An optional user-specified, uniform lamina width could subsequently be obtained through a morphological dilation operation with a symmetric circular structuring element. Inherent limitations in designing the structuring element means the diameter can only be of uneven pixel size, resulting in a uniform lamina of odd pixel width in the binary image. Having an uneven pixel size shrinks the fibre area proportionally and equally on both sides of the lamina wall, which minimises the bias. With the preferred configuration of the binary image, a boundary detection algorithm [pp651-654 of (23)] was applied, allowing the area of all objects present in the image to be calculated.

Muscle fibre type allocation

Following detection of the fibre boundary skeleton the program allows different fibre types to be classified in a user-defined manner (1, 2 or 3), allowing for tailored analysis. The mean red and green colour saturation levels were calculated for all fibres based on RGB pixel values inside their respective detected boundary. A k-means clustering algorithm (33) was applied to automatically assign all identified fibres into three types, for the purpose of this study we defined fibres according to the major phenotypes (Type I, IIa and IIb/x), based on their combined colour saturation. The algorithm performs best when distinguishing between strongly coloured fibres, and performs less well in distinguishing between non-coloured fibres (black) and weakly coloured fibres (little saturation of red or green). However, as automated classification is not infallible, the user may manually re-allocate individual fibres to a different type following manual inspection or reference to a separate look-up image. As an additional option, the user can specify any of the detected fibres

to be excluded from the statistics, e.g. due to structural abnormalities or staining artefacts. Typically, inspection of occasional ambiguous results produces a reliability of >95% compared to no user correction. Once the fibre type classification is accepted data are saved as a .txt file containing muscle fibre statistics, with an accompanying .mat file (a data file that is formatted for processing in MATLAB) that contains all the morphometric information (lamina position, fibre boundaries, centre of gravity, fibre type classification).

Modelling O_2 supply on segmented images

A graphical user interface (oxygen transport modeller; OTM) was coded in MATLAB for semi-automatic calculation of various morphometric indices, as well as computation of tissue oxygen tension based on images of muscle tissue biopsies. This code requires separate MATLAB licenses for the most recent versions of the following toolboxes: PDE, Mapping, Statistics. Importantly, the user is provided with a help menu at every stage of using the OTM package.

In step I, the user is offered the option to choose the type of oxygen supply analysis to be carried out. Three types of analysis are possible: (i) Capillary only, which entails that only capillary location is required and the surrounding tissue is modelled as homogenously consuming oxygen, with no resolution of the fibre distribution which can be used as a control for understanding the impact of fibre size and heterogeneity (ii) Capillary and Fibres, which additionally allows for interstitial spaces and oxygen uptake restricted to fibre interiors and (iii) Capillary and Fibre types, where the individual fibres can be of different types, allowing heterogeneous distributions of fibres, with the associated heterogeneous oxygen kinetics.

After loading the .mat file exported from DTect, the user can then check the quality of segmented tissue composition (Fig. 1B, D) against the biopsy image (Fig. 1A, C) for potential artefacts that may arise from image processing, with options available to manually edit capillary locations, fibre outlines, and fibre types in order to match the biopsy reference image. In step II, technical options are provided for improving the speed and accuracy of PO_2 computation by removing the digital

noise inherited in fibre outlines during the image-processing stage. Here the user is offered the options of (i) smoothing fibre outlines using a simple moving average algorithm, (ii) reducing the number of points used to interpolate the fibre outlines using the recursive Douglas-Peucker Line Simplification algorithm (14) and (iii) removing erroneous fibre-fibre overlaps by automatic application of an eraser tool. In step III, the metric dimensions of the original image biopsy are defined by the user for dimensionalising the statistical and computational model parameters that will be used in later analyses, with manual determination of the region of interest (ROI) for generating statistical measures of tissue capillary supply (Fig. 1D). Step IV provides the user the option of proceeding either to morphometric analyses based on the user-defined ROI in step III or to computational modelling of the spatial distribution of oxygen tension (Fig. 1F). Note the pipeline is designed so that data may be extracted at different stages, above, depending on the experimental design. The user specified sample area (ROI) is chosen to maximise the field of view that is sampled while maintaining an adequate guard zone to preserve the unbiased nature of sampling for fibres of differing size, and avoiding infinite capillary domains at image edges (i.e. those without converging boundaries).

Morphometric analysis of capillary oxygen supply

The first option for tissue oxygenation analysis is concerned with calculating, viewing and exporting global as well as local morphometric indices of capillary oxygen supply (Table 1). The oxygen transport modeller (OTM) program offers the user options for viewing the statistical distributions of various indices as bar-plots with adjustable number of bins (Supporting Fig. 1). Detailed morphometric supply indices (e.g. per fibre, per fibre-type, per capillary) can be exported, in tabulated form, in a .txt file for further external analyses and presentations.

Table 1. List of morphometric indices of capillary oxygen supply and defining formulae

Index	Label	Formula/Description	Units
Number of capillaries	N_{cap}	Capillary count	

Number of fibres	N_{fib}	Muscle fibre count	
Capillary density	CD	$\text{CD} = \frac{N_{\text{cap}}}{\text{Area(tissue)}}$	mm^{-2}
Capillary-to-fibre ratio	C:F	$\text{C:F} = \frac{N_{\text{cap}}}{N_{\text{fib}}}$	
Fibre area	FCSA	Cross-sectional area of a muscle fibre	μm^2
Fibre Region	FCSA_n	The region of the n^{th} fibre	
Capillary domain area	DOM	Cross-sectional area of a capillary domain	μm^2
Capillary domain	DOM_i	The region of the i^{th} capillary domain	
Equivalent Krogh diameter	K	$\text{K} = \sqrt{\frac{4 \times \text{DOM}}{\pi}}$	μm
Nearest neighbour distance	NND	The neighbouring capillary with shortest distance, where neighbouring capillaries are identified as those which have domains sharing an edge with the capillary in question.	μm
Domain-to-fibre ratio	DFR	Number of capillary domains overlapping a muscle fibre.	
Fibre-to-domain ratio	FDR	Number of muscle fibres overlapping a capillary domain.	
Local capillary-to-fibre ratio of the n^{th} fibre	LCFR_n	$\text{LCFR}_n = \sum_{i=1\ldots Ncap} \frac{\text{Area}(\text{DOM}_i \cap \text{FCSA}_n)}{\text{Area}(\text{DOM}_i)}$	
Local capillary density of the n^{th} fibre	LCD_n	$\text{LCD}_n = \frac{\text{LCFR}_n}{\text{Area}(\text{FCSA}_n)}$	μm^{-2}
Logarithmic SD of domain areas	logSD	Standard deviation of the logarithm of the capillary domain area per square micron, $\text{DOM}/\mu m^2$	

All calculations are based on the selection criteria of capillaries and fibres within the ROI. $Area$ denotes the cross-sectional area, ∩ denotes the spatial intersection, $\sum_i$ denotes summing over the list $i = 1, 2, 3, \ldots,$

284

285 *Computational modelling of oxygen tension*

286 This part of the OTM program applies mathematical and computational frameworks to generate

287 theoretical predictions of the cross-sectional distribution of oxygen tension in a muscle biopsy.

288

289 In step I, the user supplies relevant biophysical parameters (Table 2) to be used in the
290 mathematical model detailed below. Here, the user can use default parameters for uniform
291 muscles (1, 32) or supply parameters either by manual entry or by uploading a formatted .txt file.
292 The user is then able to provide further biophysical parameters: (i) exercise level, where $MO_{2,max}$
293 (the maximal rate of oxygen consumption) is chosen according to the exercise level (resting, low,
294 moderate, or high), (ii) tissue heterogeneity (uniform or fibre-specific parameters), and (iii) level of
295 differential extraction of oxygen (low, moderate, high) among fibre types.
296
297 In step II, a triangular mesh is generated using the PDE toolbox in MATLAB (*via* the built-in
298 command 'generateMesh', with further details in the Appendices) to capture structural intricacies of
299 a cross-section of muscle fibres for later finite-element computations (Fig. 1E). The mesh is
300 sufficiently dense in the vicinity of structures where oxygen gradient is expected to be relatively
301 high (e.g. capillary and fibre borders; 41), with zoom options to view details of the mesh near such
302 structures. The size of the generated mesh varies with complexity of muscle fibre and capillary
303 organisation, potentially leading to large mesh datasets. To accommodate studies investigating the
304 effect of different parameter sets and/or exercise level, there is an option to store large datasets
305 generated for the geometrical mesh as well as reload previously stored datasets.
306
307 In step III, the triangular mesh is used to compute the spatial distribution of PO_2 (oxygen tension)
308 and MO_2 by applying a mathematical modelling framework (details below) that is implemented via
309 the finite-element computational framework of the PDE toolbox in Matlab. The cross-sectional PO_2
310 and MO_2 distributions are visualized on image biopsy sections using heat maps (Fig. 1F) with
311 options for pre- and user-defined maximum and minimum PO_2 levels to obtain an appropriate
312 dynamic range. In addition, the user can export heat maps of PO_2 and MO_2, relative frequency
313 plots of PO_2 and MO_2, and a .txt file tabulating global tissue and fibre-specific statistics for PO_2 and
314 MO_2 (e.g. Table 5, Fig. 6: computed examples from samples from a pre- and post-immobilisation
315 study).
316

In step IV, the user is able to view PO_2 flux lines (Supporting Fig. 2) as a way of assessing the accuracy of capillary domains in representing supply/demand mismatches. PO_2 flux lines are determined by the following system of ordinary differential equations:

$$\frac{d\bar{x}}{dt} = \nabla p \quad (1)$$

where p is the computed oxygen tension, and $\bar{x}$ is the 2D trace of a flux line (2). To generate flux lines the user is prompted to supply a set of parameters for solving the model equations, with the option of using default parameters. Note that choosing the appropriate numerical values may require trial-and-error before smooth, complete flux lines are obtained.

Mathematical modelling framework

As noted previously, using the geometric mesh generated from histological images (Fig. 1D) a direct exploration of the oxygen transport capacity of tissue can be made using a mathematical modelling framework, based on finite element analysis, with physiological parameters applied to structural objects (Fig. 1E-F). Oxygen transport within skeletal muscle tissue is considered to be a 2D process in that local gradients along capillaries are theoretically estimated to be of insufficient scale to be relevant [2], and completed through three exchange pathways: free O_2 diffusion according to partial pressure gradients, facilitated diffusion *via* myoglobin, and consumption within muscle fibres primarily driven by Michaelis-Menten kinetics (22). Intravascular boundary conditions (e.g. O_2 exchange with interstitial fluid or fibre boundaries) are accounted for in the model through a Robin boundary condition at the capillary wall (3), which balances flux with the O_2 partial pressure drop across the capillary wall. The primary regions of O_2 demand are the interstitial space (low) and muscle fibres (variable) that are accommodated with the assumption that the interstitial space diffusivity and solubility of O_2 are equal to those of the neighbouring fibres, and different fibre types are assigned individual physiologically informed values for oxygen uptake and myoglobin concentration (Table 2).

The tissue oxygen tension (PO_2) is calculated from the following oxygen transport balance equations:

$$\nabla \cdot \Big[\underbrace{D(x)\nabla(\alpha(x)p)}_{\textbf{free diffusive flux}} + \underbrace{C^{Mb}(x)D^{Mb}(x)\left(\frac{dS_{Mb}}{dp}\nabla p\right)}_{\textbf{myoglobin-facilitated flux}}\Big] = \underbrace{M(x,p),}_{\textbf{tissue consumption}} \quad x \in \Omega, \tag{2}$$

$$n_i \cdot [D(x)\nabla(a(x)p)] = k\big(p_{cap_i} - p\big), \quad x \in \partial\Omega_i, \tag{3}$$

$$n_{tissue} \cdot [D(x)\nabla(a(x)p)] = 0 \quad x \in \partial\Omega \tag{4}$$

$$S_{Mb}(p) = \frac{p}{p + p_{50,Mb}}, \quad M(x,p) = \frac{M_0(x)p}{p + p_c}, \quad x \in \Omega, \tag{5}$$

where Ω denotes the entire area of tissue in the digital image of the muscle biopsy, excluding capillary lumen (Ω_i, with normal n_i) with the outer boundary of the tissue ($\partial\Omega$, with normal n_{tissue}), S_{Mb} is the equilibrium saturation of myoglobin, $p_{50,Mb}$ is the PO_2 in tissue at half myoglobin saturation, p_c describes the tissue PO_2 reflective of the partial pressure scale where mitochondria are no longer able to extract oxygen at maximal rate, M is the rate of oxygen consumption within the tissue, and M_0 is $MO_{2,max}$ (3). All remaining physiological parameters are detailed in Table 2.

The diffusive response of the system occurs on a timescale of

$$\frac{L_{IC}^2}{4D} \sim \frac{(50\ \mu\mathrm{m})^2}{4 \times 2 \times 10^{-9}\mathrm{m^2 s^{-1}}} \sim 0.025\mathrm{s},$$

where L_{IC} is the scale of the intercapillary distance, which is on the scale of 50 microns, based on the time taken for a diffusing particle, i.e. a random walker, to possess a root mean square displacement of L_{IC}. This is far smaller than the timescale of system adjustment, such as tissue

remodelling, and hence the (qausi)-static approximation is extremely accurate and temporal derivatives can be safely neglected.

Note that the absence of a myoglobin flux at the fibre boundary in the above equations entails that the implicit assumption of equilibrium between oxygen and myoglobin cannot hold in a region very close to the fibre boundary. However, the extremely limited geometrical extent of this region is so small that its neglect in the above system is of no consequence to robust approximation, as for instance demonstrated in the exploration of oxygen transport boundary layers by Whiteley et al. (44). Furthermore, the assumption of zero flux at the edge of the region of interest introduces a modelling error as there may be a small physiological flux present. However the lengthscale on which the impact of the boundary, or a capillary, decays is given by balancing the diffusive flux with the decay in Eqn (2), which reveals

$$L_{decay} \sim \left(\frac{D\alpha p_{cap_i}}{M_0}\right)^{1/2} \sim 140 \text{ microns.}$$

Hence more than a few hundred microns away from the boundary the impact of the boundary is predicted to be small by scaling arguments, and this is explicitly confirmed numerically in previous work [2].

Table 2. Physiological parameters for homogenous and mixed muscle oxygen modelling

Parameter	Symbol	Uniform phenotype	Fibre Type			Units
			I	IIa	IIb/x	
O_2 demand	M_0	15.7	15.7	13.82	7.85	10^{-5}ml O_2/ml s
Mb concentration	C^{Mb}	10.2	10.2	4.98	1.55	10^{-3}ml O_2/ml
O_2 solubility	α	3.89 x 10^{-5}	3.89 x 10^{-5}			ml O_2/ml mmHg
O_2 diffusivity	D	2.41 x 10^{-5}	2.41 x 10^{-5}			cm^2/s
Mb diffusivity	D^{Mb}	1.73 x 10^{-7}	1.73 x 10^{-7}			cm^2/s
Mass transfer coefficient	k	4.0 x 10^{-6}	4.0 x 10^{-6}			ml O_2/cm^2 mmHg
Intracapillary PO_2	p_{cap_i}	30	30			mmHg
Mb half-saturated PO_2	$p_{50,Mb}$	5.3	5.3			mmHg
PO_2 at half demand	p_c	0.5	0.5			mmHg
Capillary radius		1.8-2.5 x 10^{-4}	1.8-2.5 x 10^{-4}			cm

Default biophysical parameters within oxygen transport modeller, with user versatility to amend parameters. Table adapted from (4)

Worked examples of distinct physiological and pathological tissue

(1) Heterogeneity of rat skeletal muscle composition

Tibialis anterior (TA) is the predominant ankle flexor muscle located in the anterior compartment of the rat hind limb. The TA has a heterogeneous distribution in muscle fibre type and capillary supply that give rise to phenotypically distinct compartments (13, 15, 19), a deep oxidative core and superficial glycolytic cortex (Fig. 2).

The global composition of rat TA is presented, using numerical indices based on global measures for the two compartments (Fig. 3A-C). Moving to an area-based analysis, we define the capillary supply region as the area of tissue closer to an individual vessel than any other. The resultant boundary, calculated by bisecting intercapillary distances for nearest neighbour vessels, identifies the capillary domain (19, 26). The frequency distribution of these domains shows a distinctive difference between the two compartments of TA (Fig. 3D), with average capillary domain area significantly lower in the core compared to cortex (974 $\pm$ 193 μm^2 *vs.* 1789 $\pm$ 525 μm^2, $t_{3.796} = -2.916$, $P = 0.046$). Spatial heterogeneity of capillary supply is inferred from the logarithmic normal distribution by calculating the standard deviation of log-transformed area (logSD). In the oxidative core capillary supply is more homogeneously distributed than in the glycolytic cortex; logSD = 0.151 $\pm$ 0.016 *vs.* 0.166 $\pm$ 0.008, respectively ($t_{4.459} = -1.742$, $P = 0.149$). The non-integer index of local capillary to fibre ratio (LCFR = cumulative fraction of individual domains overlapping a fibre; see Table 1) allows calculation of the average supply to a fibre relative to capillary domain area (19), which is globally approximated by the ratio of mean fibre cross sectional area and mean domain area. Normalising this index (dividing LCFR by fibre area) provides a local scale-

412 independent measure of capillarity, giving a local capillary density (LCD, capillary supply
413 equivalent per unit area of fibre) specific to individual fibres (see Table 1 for formulae).
414
415 These indices of capillary supply have been partitioned into individual compartments only (Table
416 3); a more in-depth level of analysis is available, where greater computational resolution
417 distinguishes changes of an individual fibre type (demonstrated in the second worked example).
418
419

420 **Table 3. Scale-independent measures for the core and cortex of the rat TA**
421

	Core	Cortex
LCFR	1.80 ± 0.40	1.34 ± 0.20
B	0.0008	0.0004*
R^2	0.51722	0.35873
LCD (mm^{-2})	1058 ± 195	602 ± 122 *
B	-0.1025	-0.1083
R^2	0.20222	0.04868

LCFR, local capillary to fibre ratio; LCD, local capillary density. B, slope coefficient for plots in Fig. 3F,G of LCFR and LCD vs FCSA; R^2, Coefficient of determination. Mean ± SD (n=4); * $P < 0.05$ core *vs.* cortex.

422
423

424 *(2) Human muscle biopsies following two weeks immobilisation*

425 Understanding not only the physiological response to imposed challenges (adaptive remodelling),
426 but also that of pathological remodelling is critical to the development and prescription of effective
427 therapeutic exercise protocols. Prolonged bed rest is a potent stimulus for reduction in muscle
428 mass, force generating capacity and fatigability, all of which are amplified in the elderly (25, 35).
429 Muscle biopsies from the *vastus lateralis* were taken at day 0 (pre-cast) and 14 (post-cast) (9).
430 Sections were treated as above, and images processed for analysis (Fig. 4).
431

Although underpowered for statistical purposes, the expected trend for muscle atrophy is evident and clearly diagnostic (Fig. 4B, Fig. 5C). As there was no compensatory change in C:F (Fig. 5A), the functionally relevant CD consequently increased (Fig. 5B). Note this increase in apparent capillarity is entirely explained by the muscle, rather than microvascular response to immobilisation. The numerical proportion of fibres was altered in favour of Type IIa, whereas the greatest change in areal composition was found for Type IIx fibres (Fig. 5E). Given these changes, it is impossible to ascertain from global values whether or not local compensatory mechanisms have been evoked, emphasising the utility of the current multi-level analytical approach.

Consistent with a higher CD, the mean domain area (for grouped data) decreased from 3428.3µm to 2767.6 µm, with more capillaries on average supplying a smaller volume of tissue. Interestingly, heterogeneity of capillary spacing (logSD) also decreased (from 0.167 to 0.143; Fig. 5D), indicating a more similar intercapillary distance underpinning local O_2 diffusion. Indeed, for Type I fibres both LCFR and LCD were increased, for Type IIa fibres LCFR was unchanged but LCD increased (i.e. while local capillary proximity was maintained, potential supply per unit area of fibre was greater). In contrast, for Type IIx fibres there were reciprocal changes in the indices of local capillary supply (Fig. 5F-I, Table 4).

Table 4. Local capillary supply indices for pre *vs.* post immobilisation muscle biopsies

	Pre immobilisation	**Post immobilisation**
Global		
LCFR	1.69 ± 0.08	1.73 ± 0.07
LCD (mm^{-2})	281 ± 61	362 ± 50
Type I		
LCFR	**1.72 ± 0.23**	**1.84 ± 0.16**
B	0.0001	0.0002 *
R^2	0.19321	0.25169
LCD (mm^{-2})	**285 ± 67**	**376 ± 50**
B	-0.0199	-0.029
R^2	0.18825	0.13153
Type IIa		
LCFR	**1.71 ± 0.23**	**1.70 ± 0.21**

B	0.0001	0.002 *
R^2	0.2611	0.42676
LCD (mm^{-2})	**278 ± 63**	**359 ± 55**
B	-0.0193	-0.0246
R^2	0.23833	0.16305
Type IIx		
LCFR	**1.54 ± 0.42**	**1.35 ± 0.03**
B	0.0002	0.0001
R^2	0.74529	0.01974
LCD (mm^{-2})	**240 ± 27**	**307 ± 56**
B	-0.0065	-0.0456
R^2	0.08351	0.28654

LCFR, local capillary to fibre ratio; LCD, local capillary density. B, slope coefficient for plots against Capillary Domain Area in Fig. 5 (F-I); R^2, Coefficient of determination. Mean ± SD (n=4); * $P < 0.05$ Pre *vs.* Post.

Muscle oxygenation

Oxygen tension across muscle is dependent on both capillary supply and fibre demand, and influenced by spatial distribution of both elements (2, 4, 32). Using published estimates of capacity for supply and demand, the integrative response to low and high oxygen consumption can be modelled (Fig. 6). Note that fibre atrophy following immobilisation tends to ameliorate the apparent supply deficit under conditions of simulated muscle activity (Table 5). The optimisation of oxygen supply and demand by integration of capillary and fibre distributions is evident from a similar oxygen tension for each fibre type at rest, a good example of structure-function homeostasis (Table 4). Interestingly, the differential atrophy among fibre types is reflected in the extent to which fibre PO_2 is calculated to change on exercise after 14 days immobilisation (Table 5), thereby identifying local sites of likely dysfunction that may be specifically targeted in subsequent therapies.

Table 5. PO_2 predictions for one individual, pre *vs.* post immobilisation values used to generate Figure 6

Simulation	Pre	Post
Resting O_2 consumption		

Tissue PO_2 (mmHg)	26.27 ± 1.19	26.58 ± 0.93
Type I PO_2 (mmHg)	26.36 ± 1.06	26.57 ± 0.91
Type IIa PO_2 (mmHg)	26.11 ± 1.12	26.58 ± 0.83
Type IIx PO_2 (mmHg)	25.33 ± 1.57	25.98 ± 1.03
% Hypoxic tissue	0	0
Maximum O_2 consumption		
Tissue PO_2 (mmHg)	14.58 ± 5.78	15.90 ± 4.58
Type I PO_2 (mmHg)	15.21 ± 5.13	16.03 ± 4.44
Type IIa PO_2 (mmHg)	13.40 ± 5.44	15.62 ± 4.13
Type IIx PO_2 (mmHg)	9.63 ± 7.19	12.13 ± 4.94
% Hypoxic tissue	2.43	0.51

Mean ± SD; Hypoxia is user-defined, and describes the percentage of tissue area that has a PO_2 below that value, in this case <0.5mmHg O_2.

Discussion

Methodological considerations

There is an increasing body of experimental data derived from muscle histology, with a range of labelling methods contributing to variability in published results. Unacceptably laborious image processing methods reduce the scope for comparative analyses (in our experience just performing domain analysis for capillary distribution is ~5x slower, and fibre type - capillary interactions likely to be ~20x slower, using manual analysis), and underpowered studies may lead to ambiguous outcomes. We have developed a robust histological fluorescent staining protocol for identification of muscle fibre phenotype and microvascular content within rodent and human tissue. In principle this would also work for non-fluorescent staining, although fluorescent staining gives a better signal to noise ratio, avoiding limitations to chromogenic stains such as spectral overlap. Clearly, the better the staining is, i.e. the more homogeneous and noiseless it is, the easier fibre type segmentation is to perform. For good image quality the similarity in output among different users is very high, as it requires little manual intervention, amounting to 1-2 mins at most.

Although recent progress in computational modules have seen the development of semi-automatic muscle analysis code, the range of measurements involved and quality of data output has been limited (34, 36, 39). In conjunction with histological labelling we developed a semi-automated

detection software for the identification of fibre borders and fibre types that allows co-localisation of capillaries within an anatomically appropriate skeleton. Subsequently, a digitised mesh representative of tissue geometry is created, which provides the framework for improved spatially-resolved data acquisition, and the possibility of realistic modelling of oxygen tension based on images of muscle biopsies (3, 46). With the availability of both a pipeline for generating spatially-resolved data and the mathematical models for accommodating fine tissue scale (4), we developed a graphical user interface for computational modelling of muscle tissue oxygenation based on biopsy images.

Using the principles of coordinate-dependent stereology we utilise a systematic random sampling regime that accommodates regional heterogeneity. Given that between-individual variance is greater than within-individuals, we emphasise the need for high throughput analysis to accommodate a large sample size rather than increasing the relatively small size of the ROI. Previous studies have shown that increasing sampling within an individual have minimal effects on the outcome. However, within disease populations this variance may be greater, and the experimental protocol needs to recognise this.

Fibre type composition

Accurate quantification of skeletal muscle composition is labour intensive, and it is sometimes difficult to reconcile results from different studies. The literature has become dominated by concerns about pure and hybrid phenotypes (a single fibre expressing more than one MHC isoform) (8). There are a variety of monoclonal antibodies developed to probe for various configurations of these phenotypes, which allow muscle fibre type compositions to be determined (8, 24). However, the functional capacity of these scarce hybrid fibres is still to be determined, and the relevance to overall muscle phenotype is debatable. A more broadly applicable method may be to use an oxidative continuum to classify fibres, e.g. using data from succinate dehydrogenase and α-glycerophosphate dehydrogenase activity in conjunction with the various MHC monoclonal antibodies (8).

519

520 Using this continuum (left most oxidative, moving to entirely glycolytic, Fig. 7) it is possible to
521 accommodate the categorisation of three major fibre types. The flexibility of the programme to
522 allow user-defined classifications will permit groupings for undifferentiated hybrid fibres, if required.
523 Accordingly, the purpose of the immuno/histochemical protocol is to provide a high throughput
524 method of fibre type differentiation, in combination with our semi-automated detection system,
525 analysis and modelling package.

526

527 *Experimental data*

528 The underlying heterogeneity of muscle composition is often under-appreciated, which descriptions
529 of homogeneous phenotype (even in mixed muscles) not uncommon. Appreciating the functional
530 correlates of variability in both fibre (13) or capillary (19) distribution requires a detailed analysis of
531 the spatial correlation and adaptive interaction between the structural correlates of aerobic
532 capacity (15, 19).

533

534 Such data illustrate the manner by which microvascular delivery of oxygen and other substrates,
535 and removal of metabolites, is partitioned among both muscle region and fibre type. Of note is the
536 extent to which global values smooth local differences in functional capillary supply, and hence are
537 less sensitive to tissue remodelling during physiological adaptation or pathological dysfunction.
538 The two most commonly reported indices of global capillary content are CD and C:F (16) but these
539 measures are scale-dependent (affected by alterations in muscle fibre size), with important
540 implications when describing angiogenesis in skeletal muscle as this is often accompanied by
541 changes in FCSA. Hence, applying such higher resolution analysis may afford a more sensitive
542 diagnostic option than currently available.

543

544 The regional differentiation of hindlimb extensor muscles provides a good example of how varied
545 the local environment can be for examples of a given fibre type in different locations. The hope is
546 that with such information now available, we may develop a better understanding of e.g. the

547 principal determinants of exercise capacity, and the primary drivers of adaptive response. Indeed,
548 recent studies examining muscle oxygenation confirm that this is highly correlated with
549 morphometric indices, especially capillary distribution (45).
550
551 Bed rest has been shown to have a pronounced debilitative effect on skeletal muscle mass and
552 aerobic capacity (7, 21, 25, 42). Inactivity (hypokinesia) results in atrophy of muscle fibres,
553 alteration in blood flow kinetics and reduced oxidative capacity, which subsequently impairs
554 muscle performance capacity, especially in the elderly (25). We utilised a unilateral limb
555 immobilisation cast to mimic bed-rest for two weeks to investigate the effect on muscle phenotype
556 and oxygen delivery kinetics (9, 40).
557
558 Following two weeks of lower-limb casting the *vastus lateralis* atrophied, with a 31% decrease in
559 mean fibre area, with Type II fibres showing the largest degree of atrophy. These data are in line
560 with those reported previously (40), although others have reported a larger atrophy of Type I fibres
561 over longer durations (6, 27, 41). There was no evident rarefaction of the capillary bed, however
562 overall atrophy of muscle fibres resulted in a higher CD. A similar response has been shown in
563 cold acclimated hamsters, that manage to reduce oxygen diffusion distance through reduction in
564 FCSA and increasing CD (13). Mean capillary domain area decreased, with an improved
565 homogeneity of capillary supply that improved LCD across all three major fibre types. The reduced
566 diffusion distance and subsequently improved local capillary supply area suggest a better PO_2
567 status across the tissue when modelled at high intensity exercise levels, and reduced proportion of
568 the tissue considered to be hypoxic (in this model hypoxia was considered to be represented by a
569 tissue PO_2 <0.5 mmHg). This adaptive remodelling appears to preserve O_2 supply capacity of the
570 tissue, possibly as a compensatory mechanism. As the tissue also has a reduced capacity to
571 utilise O_2, due to decreased oxidative enzyme content and mitochondria (10, 28), this higher PO_2
572 and subsequent potentially greater O_2 flux would help maintain functionality of remaining
573 mitochondria and likely allow them to work optimally (11).
574

575 *Adaptability and versatility of the analysis package*

576 The user is required to provide information about the type of tissue geometry to be processed. The
577 current image segmentation algorithms can process three types of image: (i) capillary location
578 only, (ii) capillary location and fibre outlines, and (iii) capillary location with fibre outlines and
579 defined fibre type (Fig. 8). Capillary location alone (Fig. 8A) allows for global morphometric indices
580 such as capillary density (CD) and mean intercapillary distance (ICD) to be quantified, as well as
581 the calculation of capillary domains and the beginning of capillary heterogeneity analysis (17).
582 Capillary co-location with fibre boundaries (Fig. 8B) gives rise to the generation of local non-integer
583 based indices, and allows for the modelling of capillary supply regions assuming homogeneous
584 oxygen consumption, such as found in cardiac tissue (2). Incorporating additional heterogeneities
585 in oxygen uptake *via* fibre-type allocation (Fig. 8C) allows the generation of fibre type specific, local
586 capillary indices and subsequent modelling of tissue PO_2 (4).
587
588 The packages are assembled in such a way that output files are generated at each stage: fibre
589 type composition and morphometric details, capillary and fibre global indices, fine-scale non-
590 integer local capillary indices, and finally tissue PO_2 modelling. This allows flexibility in extraction of
591 morphometric data at the level desired for a particular study design. However, given the ease of
592 data acquisition and speed of the data pipeline it is plausible to generate the full range of
593 morphometric indices with minimal time penalty, thereby allowing observation-driven explorations
594 and more extensive testing of generated hypotheses. The local indices of capillary supply are able
595 to identify the onset of fine-scale changes that occur during physiological adaptation (e.g. training
596 response) and pathological remodelling (e.g. capillary rarefaction), usually prior to differences in
597 global indices becoming apparent. The ability to generate these data provides the potential for
598 discovery of unknown abnormal pathological responses, and aid development of targeted
599 therapeutic treatments.
600
601 As discussed above, some longitudinal studies seek to identify transient changes as part of an
602 adaptive response, and so we have incorporated the possibility to utilise either serial sections and

a corresponding monoclonal label for hybrid fibre types (or other molecules of interest), or an additional fluorophore may be used for four colour immunofluorescence, which may then be incorporated into the morphometric analysis. In future, the code could be modified to take other staining colours into account, with the only limitation being that the algorithm relies on lamina colour being distinct from the remaining staining.

One of the more flexible components of this project was the development of a fibre map that allowed the incorporation of physical objects (i.e. capillaries) to then be positioned and analysed at the level of individual fibres, allowing for more sensitive geometric analysis. The versatility of the capillary identification software should be of wider interest for co-localisation of other structures, allowing the geometric distribution and interactions with specific fibre types to be generated for e.g. location of myosatellite cells, infiltration of macrophages, or specificity of proteins such as the transcription factor PGC-1α (38).

Limitations of the methods and in accuracy

The primary limitation with detection software relates to quality of imported images, with variability in specificity or intensity of stains (especially in older samples) being particularly problematic, e.g. there is an apparent reduced reactivity/affinity of monoclonal antibodies to tissue that have been cut and stored for extended periods of time (over 12 months). Tissue that has been exposed to freeze thaw cycles also showed poorer staining for laminin, making automatic detection of fibre borders ineffective and difficult to define. This can lead to artefacts such as gaps that may result in automated shrinking and removal of lamina, and joining of two adjacent fibres. This requires the user to adjust the threshold or manually define those boundaries through pruning of incorrect boundaries and addition of missing segments. Initially, the laminin threshold should be determined for a given sample, using a low threshold produces noisy images that can result in erroneous fibre detection, whereas a high threshold creates gaps and unites fibres; only once an optimal threshold has been defined should manual correction be attempted.

To unambiguously define a fibre type three critical pieces of information are required: fibre size, shape and colour fill. At present there is a user-defined minimum and maximum fibre area size that establishes boundary conditions for identified fibres and inclusion in the statistical output. While differentiation between types is primarily based on colour fill of that fibre, future implementations could allow incorporation of fibre type criteria based on size and staining intensity, or to avoid fibre boundary artefacts by implementing morphometry algorithms, e.g. including only convex, smooth objects.

As with all computational studies, numerical accuracy has the potential to be a limitation. However, in practice the numerical algorithms used here, for instance finite element methods, ordinary differential equation solvers, the determination of Voronoi polygons and quadrature for integrating to find capillary domain areas are well understood. Previous studies routinely confirm (2,3) that such techniques perform at substantively greater accuracy that the two significant figures typically required to ensure results are robust to numerical error. Parameter uncertainty, if it is present, may require confirming results are robust across a range of parameters before drawing conclusion. However, a prospective source of error would be missed capillaries in the image analysis, as previous studies as emphasised a sensitivity of the summary statistics for capillary domains and trapping regions to capillary rarefaction (2,3,4).

A further limiting aspect of the framework is the use of two-dimensional cross sections. The benefit of three dimensional studies is highly questionable compared to the resource implications and uncertainties that would be introduced. Indeed, the statistical argument to adopt such an approach for muscle is not compelling; 3D analysis only reduces error if the 2D approach lacks rigour, which we avoid (geometric probability assumptions are realised etc.). Even if the technical details of imaging and segmenting a z-stack of tissue proved to be possible without significant error (e.g. serial section registration and cross-correlation between objects, inherent assumptions about tissue geometry), there is no physically motivated and self-evident boundary conditions at the end of the stacks for oxygen transport simulations of skeletal muscles. Hence, such simulations would

be prone to errors from assumptions about boundary conditions, while Voronoi polyhedra will extensively extend into the tissue domain along the axis of the muscle fibres, corrupting capillary domain statistics with boundary artefacts. Thus, the work is therefore restricted to tissue, such as muscle, where variation in the out-of-plane direction is on a longer lengthscale than that of $L_{decay} \sim 140\ \mu\mathrm{m}$ according to scaling arguments. Consequently, the technique cannot be applied to tissues more generally.

For DTect, the computational effort of course varies with the image size, and the relationship with amount of RAM available. We have implemented the tool on personal laptops, but recommend using a desktop PC with a setup of at least 3.3 GHz clock speed, 16 Gb RAM, and 1 Tb memory, which is within specification of off-the shelf laptops and thus standard computing facilities.

Conclusions

We have designed a robust histological protocol and analysis package based on Matlab code that will be free to download and use. The data pipeline allows for flexibility in morphometric indices acquired, and provides a more comprehensive overview of microvascular supply and skeletal muscle phenotype than is currently available. The potential for higher spatial resolution data may have an impact on statistical power within a study, and as such reduce the number of animals required for experiments (supporting consideration of 3Rs in ethical approvals). As such, the development of this image processing and computational methodology will likely prove to be valuable with scientific, economic and ethical implications.

Appendices

Meshing

For meshing, the PDE toolbox in MATLAB utilised in the presented pipeline uses the Delaunay triangulation algorithm to discretize the domain into a number of linear triangular elements, finite

687 elements, with curved boundaries approximated by piecewise linear boundaries. An initial domain
688 discretization is generated by calling the built-in function INITMESH. In addition, this initial mesh is
689 adaptively refined by using the built-in function ADAPTMESH. At each refinement stage, *a*
690 *posteriori* error estimates are used to select candidate mesh elements for further refinement if they
691 contribute an error larger than a pre-set tolerance level, thus generating a variable mesh density
692 based on the properties of the solution, rather than a manual assignment of mesh density.
693
694 The number of elements has been found to be linearly correlated with the number of digitized
695 fibres in an image. This correlation remains consistent under the image processing algorithms we
696 apply for elimination of the image-segmentation noise and reduction of the number of vertices of
697 each fibre. The images considered in the worked examples contain 80-90 fibres, which is
698 equivalent to 420 – 450 thousand mesh elements.
699
700 *Generating flux lines*
701 The OTM package allows the user to generate oxygen flux lines by numerically integrating the
702 system in Equation (1). To proceed with numerical integration the following four parameters are
703 needed:
704 1. Termination time: the total integration time allowed for a streamline to travel.
705 2. Step size: a discrete time-step used uniformly to successively generate the points of a flux
706 line.
707 3. Flux lines per capillary: the number of flux lines desired around each capillary (8 to 64 is
708 sufficient).
709 4. Initial distance from capillary: since each flux line begins at a capillary wall, the user may
710 choose to start generating it a bit downstream by specifying the distance of the initial point
711 on the flux line, which should be slightly greater than the capillary radius.
712 These parameters are pre-set at default numerical values but can be manually adjusted by the
713 user to improve the quality of flux lines (e.g. smoothness and length). Thus, to generate the

desired plot quality the user may adjust these parameters by trial-and-error, with suitable numerical bounds as suggested above.

Archiving

Standalone executables will be provided at the University of Oxford Research Archive on acceptance: https://doi.org/xxxxxx/xxxxxx. The current GUI for OTM was originally coded using MATLAB 8.2 (2013b). The overall version-sensitivity of the OTM package is minor, and package updates are carried out regularly to guarantee smooth operation with new MATLAB versions. A list of OTM versions along with compatible versions of MATLAB and the relevant toolboxes will be provided at this research archive link.

Acknowledgments

We would like to acknowledge help provided by Thomas Ravnholt during the development of DTect

Grants

The authors are grateful to the School of Biomedical Sciences, University of Leeds, UK for provision of a scholarship to R.W.P.K. Funding from The Danish Agency for Science Technology and Innovation (Medical Research Council, DFF-7016-00012) and the Lundbeck Foundation (R198-2015-207) is gratefully acknowledged.

Figure 1. Flow through processing of histological images. Raw image stained for fibre type composition, fibre boundary and capillaries (Type I; red fibres, Type IIa; green fibres and Type

742 IIb/x; unstained fibres) (A). Fibre boundary skeleton is automatically masked in magenta for the
743 labelled basal lamina (B). Individual capillaries are manually identified and associated with fibres
744 (numbers within fibres record the number of capillaries in contact with that fibre) (C). A digitised
745 composite of the histological sample with fibre boundaries (dark magenta lines), associated
746 capillaries (navy blue dots) and the capillary domain areas (tessellating light blue polygons) are
747 generated and a region of interest selected (green) (D). This provides input data for calculation of
748 global and local capillary indices, as well as the modelling of oxygen tension (E), with
749 pseudocolour representation of PO_2 distribution displayed (user-defined hypoxic regions shown as
750 deep blue) (F).
751
752 **Figure 1. Cross section of rat TA with representative immuno/histochemical inserts from**
753 **the deep core (A-B) and superficial cortex (C-D).** There is a distinct oxidative gradient running
754 transversely across the muscle, with the most oxidative fibres located in the core of the muscle.
755 Type I; red fibres, Type IIa; green fibres and Type IIx/b; unstained fibres.
756
757 **Figure 3. Morphometric indices for the *tibialis anterior* oxidative core and glycolytic cortex.**
758 The global morphometric indices described through capillary-to-fibre ratio, C:F (A), capillary
759 density, CD (B) and fibre cross sectional area, FCSA (C). The relative frequency of the capillary
760 domain areas present within the two compartments (D) and fibre type composition (E). Finally, the
761 distribution of local capillary to fibre ratio, LCFR (F) and local capillary density, LCD (G) relative to
762 fibre cross sectional area are shown. See Table 1 for definitions of these indices. Mean ± SD
763 (n=4), * $P < 0.05$ core (red) *vs.* cortex (blue).
764
765 **Figure 4. *Vastus lateralis* muscle biopsy cross-sections.** Example of individual muscle biopsy
766 pre (A) and post (B) immobilisation. Immuno/histochemical staining for fibre type, fibre boundaries
767 and capillary location. Note the evident atrophy following two weeks of immobilisation. Type I; red
768 fibres, Type IIa; green fibres and Type IIx; unstained fibres. Scale bar 200µm.
769

Figure 2. Global and local microvascular and muscle morphometric indices pre (solid bars) and post 14 days immobilisation (hatched bars). Capillary to fibre ratio (A), capillary density (B), fibre cross sectional area (C), relative frequency of capillary domain area (D), relative fibre area (E). Finally, the distribution of local capillary to fibre ratio and local capillary density to fibre cross sectional area at baseline (F-G) and following two weeks of immobilization (H-I), respectively. Mean ± SD (n=4); * $P<0.05$ Pre *vs.* Post. Red, Type I; Green, Type IIa; Navy, Type IIx.

Figure 6. Oxygen modelling – simulation of muscle PO_2 at rest (A pre, C post), and at MO_{2max} (B pre, D post). Note that the regions of tissue hypoxia in this model, highlighted in blue, have a PO_2 of < 0.5mmHg. See Table 4 for fibre type-specific values.

Figure 7. The spectrum of skeletal muscle myosin heavy chain phenotypes, accommodating both pure and hybrid fibres. Fatigue resistance (red) and power (blue) describe the typical functional properties of these fibre types.

Figure 8. Versatility of image input for capillary indices calculations. Individual capillary location labelled with *Griffonia simplicifolia* lectin-1 staining (A). Capillary location with fibre boundary coordinates is optional, used primarily for homogeneous tissue phenotypes (B). Finally, capillary location built onto muscle fibre boundaries with fibre type composition, allowing differential tissue oxygen consumption to be modelled (C).

References

1. **Al-Shammari A, Gaffney E, and Egginton S**. Modelling Oxygen Capillary Supply to Striated Muscle Tissues. In: Advances in Applied Mathematics. Springer, 2014, p. 13-21.
2. **Al-Shammari A, Gaffney E, and Egginton S**. Re-evaluating the use of voronoi tessellations in the assessment of oxygen supply from capillaries in muscle. Bulletin of Mathematical Biology 74: 2204-2231, 2012.
3. **Al-Shammari AA**. Mathematical modelling of oxygen transport in skeletal and cardiac muscles. University of Oxford, 2014.
4. **Al-Shammari AA, Gaffney EA, and Egginton S**. Modelling capillary oxygen supply capacity in mixed muscles: Capillary domains revisited. Journal of Theoretical Biology 356: 47-61, 2014.
5. **Andersen T, Schmidt J, Thomassen M, Hornstrup T, Frandsen U, Randers M, Hansen P, Krustrup P, and Bangsbo J**. A preliminary study: Effects of football training on glucose control, body composition, and performance in men with type 2 diabetes. Scandinavian Journal of Medicine & Science in Sports 2014.
6. **Appell H-J**. Muscular atrophy following immobilisation. Sports Medicine 10: 42-58, 1990.
7. **Berg H, Larsson L, and Tesch P**. Lower limb skeletal muscle function after 6 wk of bed rest. Journal of Applied Physiology 82: 182-188, 1997.
8. **Bloemberg D, and Quadrilatero J**. Rapid determination of myosin heavy chain expression in rat, mouse, and human skeletal muscle using multicolor immunofluorescence analysis. PloS One 7: e35273, 2012.
9. **Boesen AP, Dideriksen K, Couppé C, Magnusson S, Schjerling P, Boesen M, Kjær M, and Langberg H**. Tendon and skeletal muscle matrix gene expression and functional responses to immobilisation and rehabilitation in young males: effect of growth hormone administration. The Journal of Physiology 591: 6039-6052, 2013.
10. **Booth F, and Kelso J**. Effect of hind-limb immobilization on contractile and histochemical properties of skeletal muscle. Pfluegers Archiv 342: 231-238, 1973.
11. **Bosutti A, Egginton S, Barnouin Y, Ganse B, Rittweger J, and Degens H**. Local capillary supply in muscle is not determined by local oxidative capacity. Journal of Experimental Biology 218: 3377-3380, 2015.
12. **Ceglia L, Niramitmahapanya S, Price LL, Harris SS, Fielding RA, and Dawson-Hughes B**. An evaluation of the reliability of muscle fiber cross-sectional area and fiber number measurements in rat skeletal muscle. Biological Procedures Online 15: 1, 2013.
13. **Deveci D, and Egginton S**. Differing mechanisms of cold-induced changes in capillary supply in m. tibialis anterior of rats and hamsters. Journal of Experimental Biology 205: 829-840, 2002.
14. **Douglas DH, and Peucker TK**. Algorithms for the reduction of the number of points required to represent a digitized line or its caricature. Cartographica: The International Journal for Geographic Information and Geovisualization 10: 112-122, 1973.
15. **Edgerton VR, Smith J, and Simpson D**. Muscle fibre type populations of human leg muscles. The Histochemical Journal 7: 259-266, 1975.
16. **Egginton S**. Invited review: activity-induced angiogenesis. Pflügers Archiv-European Journal of Physiology 457: 963-977, 2009.
17. **Egginton S**. Morphometric analysis of tissue capillary supply. In: Vertebrate Gas Exchange. Springer, 1990, p. 73-141.
18. **Egginton S**. Numerical and areal density estimates of fibre type composition in a skeletal muscle (rat extensor digitorum longus). Journal of Anatomy 168: 73, 1990.

19. **Egginton S, and Ross H**. Planar analysis of tissue capillary supply. In: Seminar Series-Society for Experimental Biology. Cambridge University Press, 1992, p. 165-165.
20. **Egginton S, Turek Z, and Hoofd L**. Differing patterns of capillary distribution in fish and mammalian skeletal muscle. Respiration Physiology 74: 383-396, 1988.
21. **Gallagher P, Trappe S, Harber M, Creer A, Mazzetti S, Trappe T, Alkner B, and Tesch P**. Effects of 84-days of bedrest and resistance training on single muscle fibre myosin heavy chain distribution in human vastus lateralis and soleus muscles. Acta Physiologica Scandinavica 185: 61-69, 2005.
22. **Goldman D**. Theoretical models of microvascular oxygen transport to tissue. Microcirculation 15: 795-811, 2008.
23. **Gonzalez RC, Woods RE, and Eddins S**. Digital Image Processing Using MATLAB: Pearson Prentice Hall. Upper Saddle River, New Jersey 2004.
24. **Gregorevic P, Meznarich NA, Blankinship MJ, Crawford RW, and Chamberlain JS**. Fluorophore-labeled myosin-specific antibodies simplify muscle-fiber phenotyping. Muscle & Nerve 37: 104-106, 2008.
25. **Harper CM, and Lyles YM**. Physiology and complications of bed rest. Journal of the American Geriatrics Society 36: 1047-1054, 1988.
26. **Hoofd L, Turek Z, Kubat K, Ringnalda B, and Kazda S**. Variability of intercapillary distance estimated on histological sections of rat heart. In: Oxygen Transport to Tissue VII. Springer, 1985, p. 239-247.
27. **Hortobágyi T, Dempsey L, Fraser D, Zheng D, Hamilton G, Lambert J, and Dohm L**. Changes in muscle strength, muscle fibre size and myofibrillar gene expression after immobilization and retraining in humans. The Journal of Physiology 524: 293-304, 2000.
28. **Jansson E, Sylven C, Arvidsson I, and Eriksson E**. Increase in myoglobin content and decrease in oxidative enzyme activities by leg muscle immobilization in man. Acta Physiologica Scandinavica 132: 515-517, 1988.
29. **Kissane RWP, Egginton S, and Askew GN**. Regional variation in the mechanical properties and fibre type composition of the rat extensor digitorum longus muscle. Experimental Physiology 103:111-124, 2017.
30. **Kreuzer F**. Oxygen supply to tissues: the Krogh model and its assumptions. Experientia 38: 1415-1426, 1982.
31. **Krogh A**. The number and distribution of capillaries in muscles with calculations of the oxygen pressure head necessary for supplying the tissue. The Journal of Physiology 52: 409-415, 1919.
32. **Liu G, Mac Gabhann F, and Popel AS**. Effects of fiber type and size on the heterogeneity of oxygen distribution in exercising skeletal muscle. PloS One 7: e44375, 2012.
33. **Lloyd S**. Least squares quantization in PCM. IEEE Transactions on Information Theory 28: 129-137, 1982.
34. **Miazaki M, Viana MP, Yang Z, Comin CH, Wang Y, da F Costa L, and Xu X**. Automated high-content morphological analysis of muscle fiber histology. Computers in Biology and Medicine 63: 28-35, 2015.
35. **Morley JE, Baumgartner RN, Roubenoff R, Mayer J, and Nair KS**. Sarcopenia. Journal of Laboratory and Clinical Medicine 137: 231-243, 2001.
36. **Mula J, Lee JD, Liu F, Yang L, and Peterson CA**. Automated image analysis of skeletal muscle fiber cross-sectional area. Journal of Applied Physiology 114: 148-155, 2013.
37. **Nyberg M, Fiorenza M, Lund A, Christensen M, Rømer T, Piil P, Hostrup M, Christensen PM, Holbek S, Ravnholt T, Gunnarsson TP, and Bangsbo J**. Adaptations to Speed Endurance Training in Highly Trained Soccer Players. Medicine & Science in Sports & Exercise 48: 1355-1364, 2016.

891 38. **Selsby JT, Morine KJ, Pendrak K, Barton ER, and Sweeney HL**. Rescue of dystrophic
892 skeletal muscle by PGC-1α involves a fast to slow fiber type shift in the mdx mouse. PloS One 7:
893 e30063, 2012.
894 39. **Smith LR, and Barton ER**. SMASH–semi-automatic muscle analysis using segmentation
895 of histology: a MATLAB application. Skeletal Muscle 4: 1, 2014.
896 40. **Suetta C, Frandsen U, Mackey AL, Jensen L, Hvid LG, Bayer M, Petersson SJ,**
897 **Schrøder HD, Andersen JL, and Aagaard P**. Ageing is associated with diminished muscle re-
898 growth and myogenic precursor cell expansion early after immobility-induced atrophy in human
899 skeletal muscle. The Journal of Physiology 591: 3789-3804, 2013.
900 41. **Tomanek RJ, and Lund DD**. Degeneration of different types of skeletal muscle fibres. II.
901 Immobilization. Journal of Anatomy 118: 531, 1974.
902 42. **Topp R, Ditmyer M, King K, Doherty K, and Hornyak III J**. The effect of bed rest and
903 potential of prehabilitation on patients in the intensive care unit. AACN Advanced Critical Care 13:
904 263-276, 2002.
905 43. **Wen Y, Murach KA, Jr. IJV, Fry CS, Vickery C, Peterson CA, McCarthy JJ, and**
906 **Campbell KS**. MyoVision: software for automated high-content analysis of skeletal muscle
907 immunohistochemistry. Journal of Applied Physiology 124: 40-51, 2018.
908 44. **Whiteley JP, Gavaghan DJ, and Hahn CEW**. Mathematical modelling of oxygen
909 transport to tissue. Journal of Mathematical Biology 44: 503-522, 2002.
910 45. **Zeller-Plumhoff B, Daly KR, Clough GF, Schneider P, and Roose T**. Investigation of
911 microvascular morphological measures for skeletal muscle tissue oxygenation by image-based
912 modelling in three dimensions. Journal of The Royal Society Interface 14: 2017.
913 46. **Zeller-Plumhoff B, Roose T, Clough GF, and Schneider P**. Image-based modelling of
914 skeletal muscle oxygenation. Journal of The Royal Society Interface 14: 2017.

915

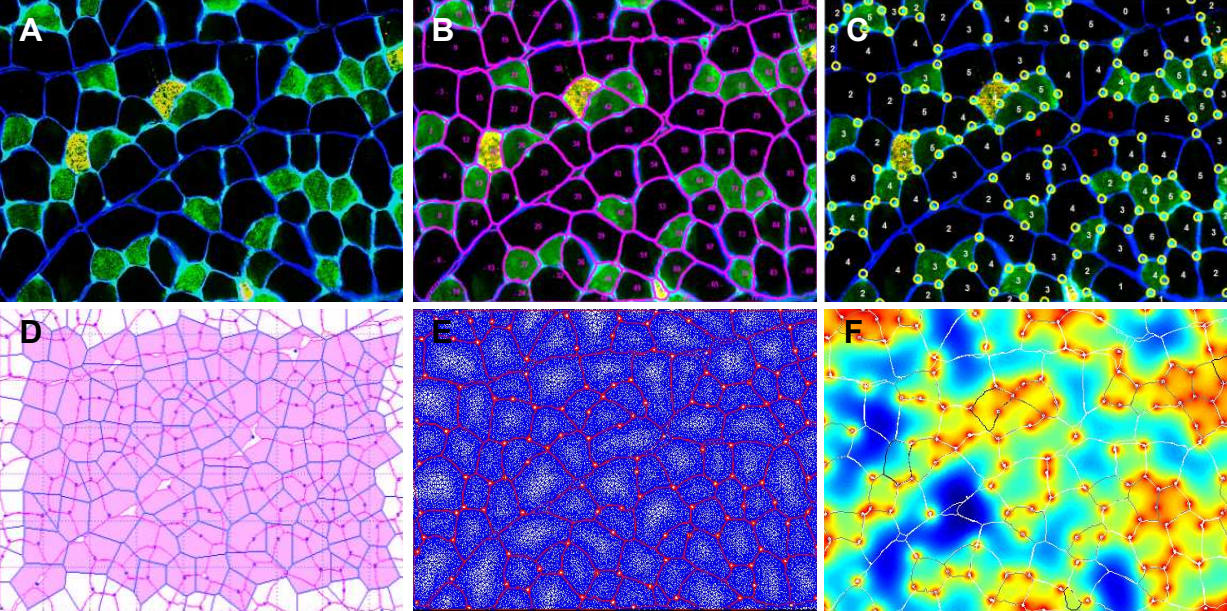
A
B
C
D
E
F

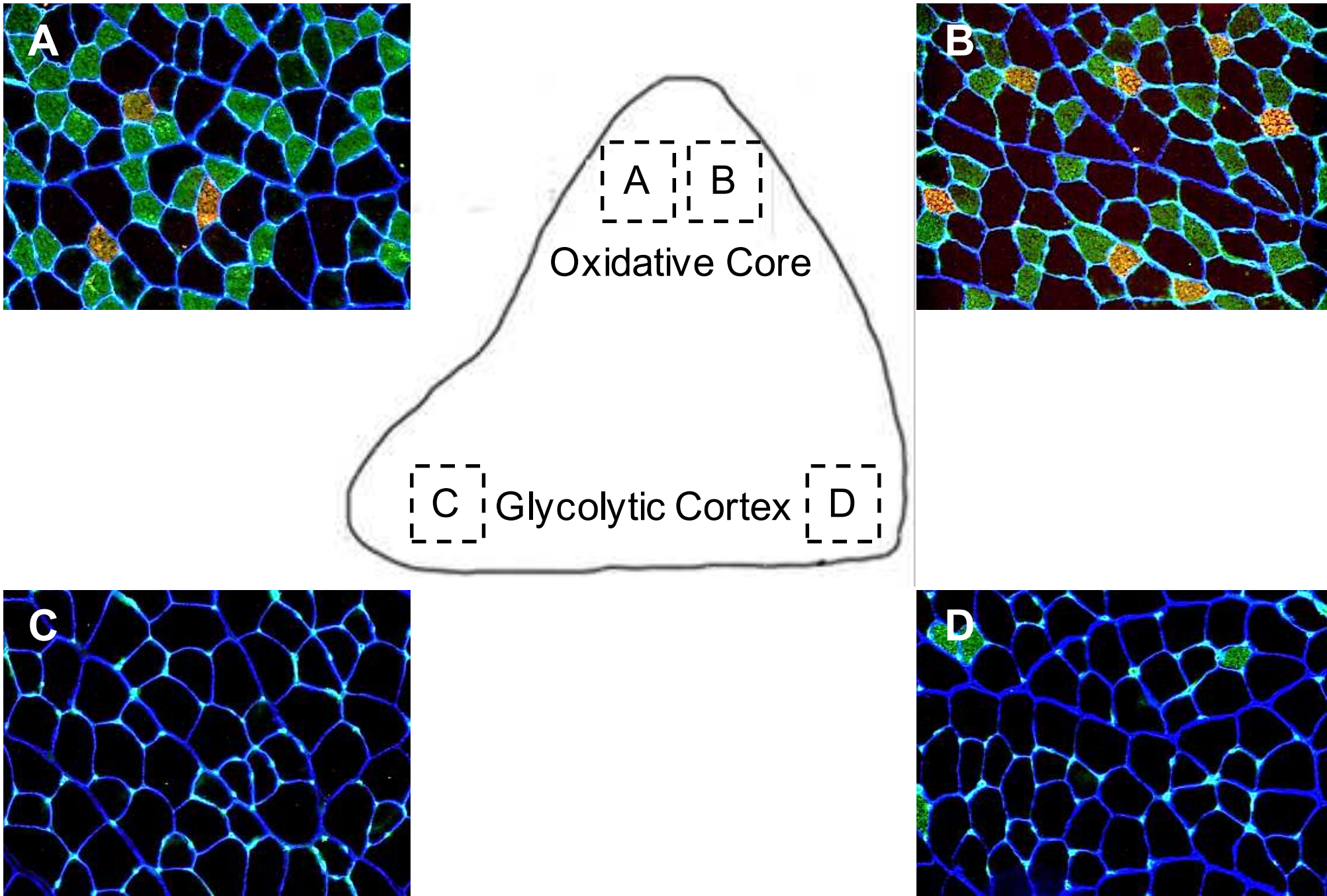
A
B
A
B
Oxidative Core
C
Glycolytic Cortex
D
C
D

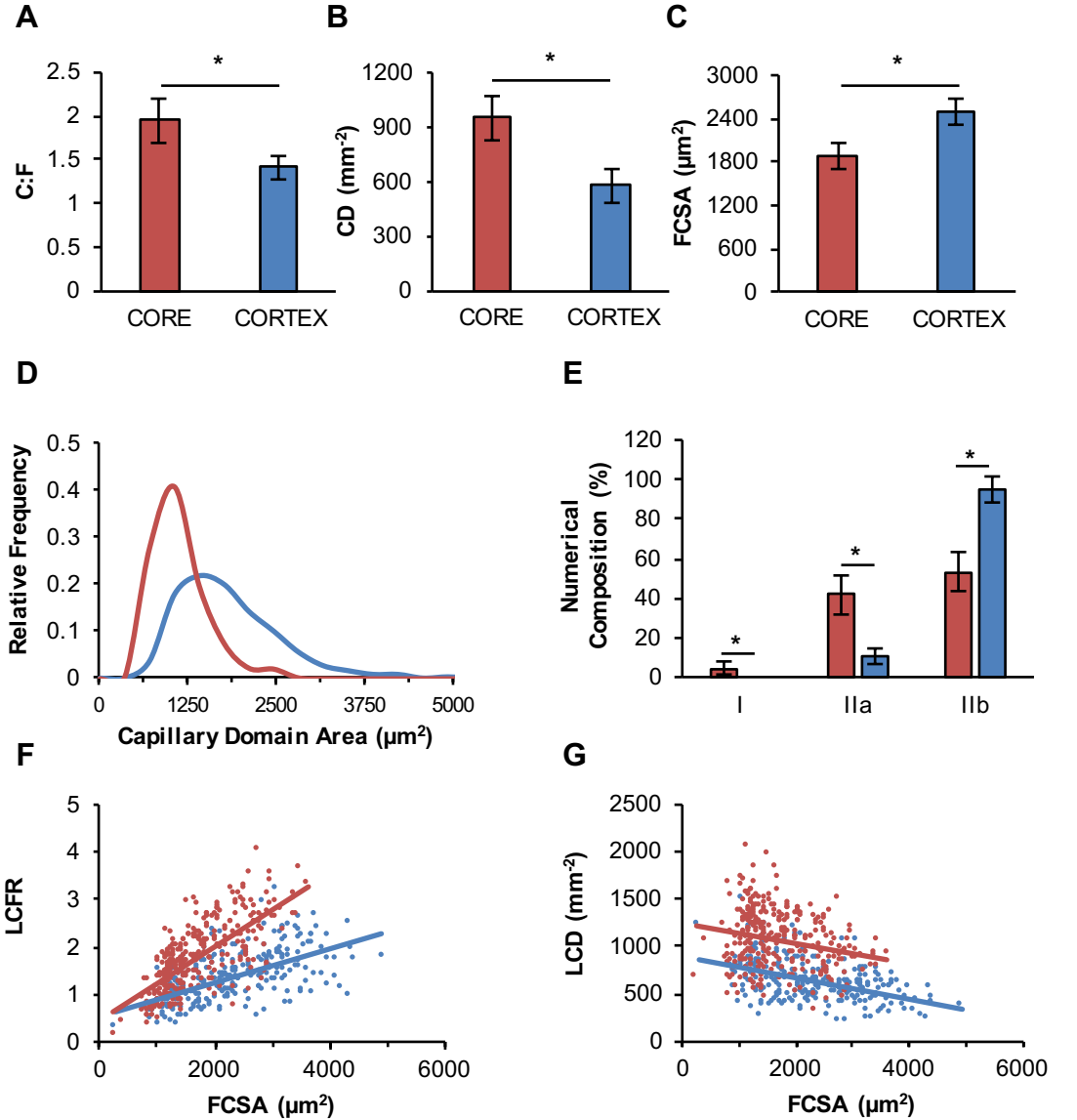
A
B
C
C:F
2.5
2
1.5
1
0.5
0
*
CORE
CORTEX
CD (mm-2)
1200
900
600
300
0
FCSA (µm2)
3000
2400
1800
1200
600
D
Relative Frequency
0.5
0.4
0.3
0.2
0.1
1250
2500
3750
5000
Capillary Domain Area (µm2)
E
Numerical Composition (%)
120
100
80
60
40
20
I
IIa
IIb
F
LCFR
5
4
3
2
1
2000
4000
6000
FCSA (µm2)
G
LCD (mm-2)
2500
2000
1500
1000
500

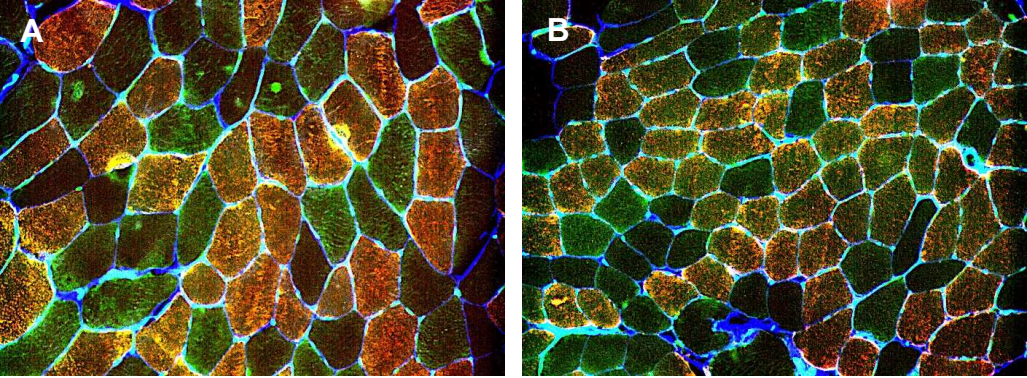
A
B

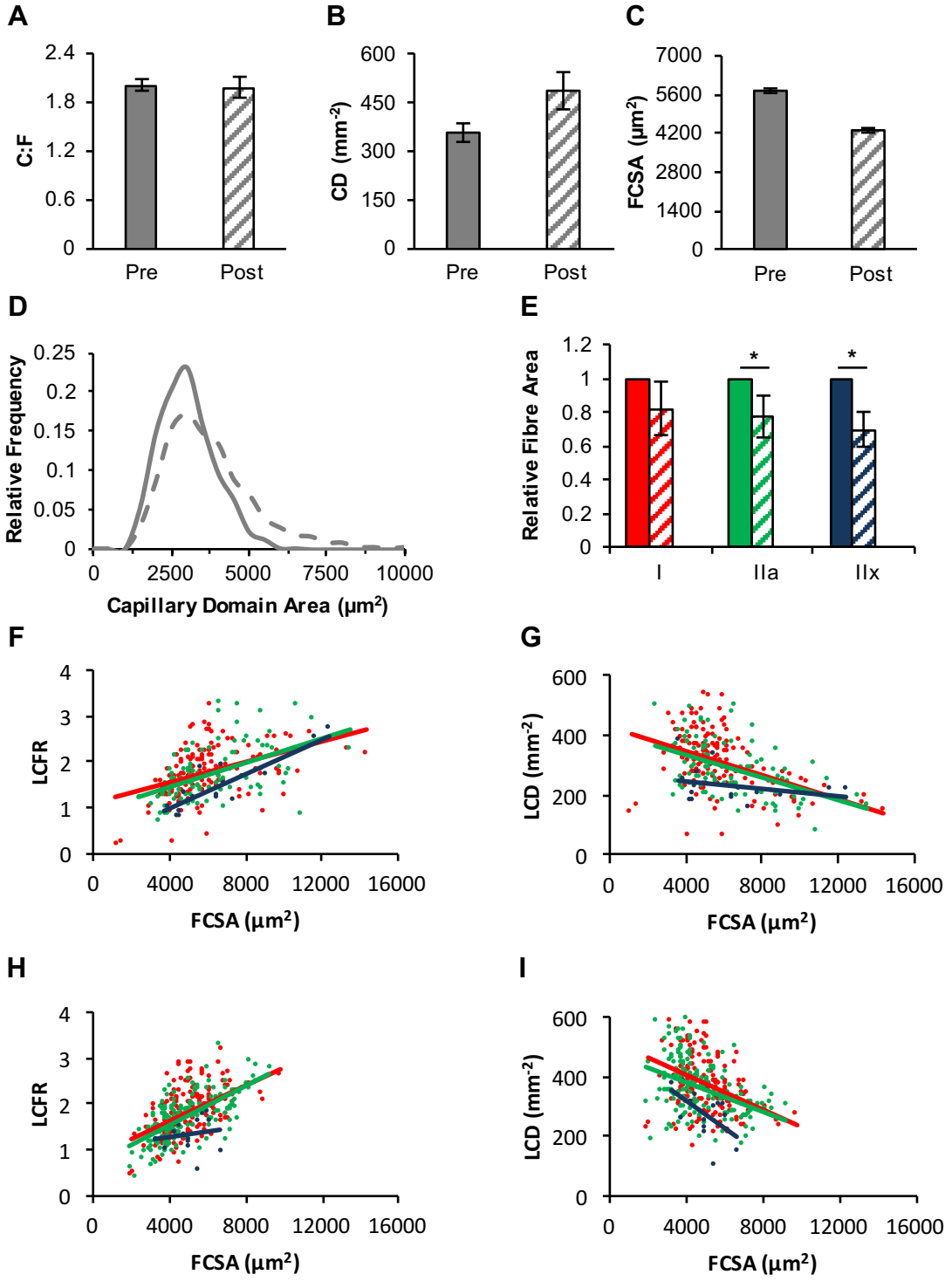
A
C:F
2.4
1.8
1.2
0.6
0
Pre
Post
B
CD (mm-2)
600
450
300
150
0
Pre
Post
C
FCSA (µm2)
7000
5600
4200
2800
1400
0
Pre
Post
D
Relative Frequency
0.25
0.2
0.15
0.1
0.05
0
0
2500
5000
7500
10000
Capillary Domain Area (µm2)
E
Relative Fibre Area
1.2
1
0.8
0.6
0.4
0.2
0
*
*
I
IIa
IIx
F
LCFR
4
3
2
1
0
0
4000
8000
12000
16000
FCSA (µm2)
G
LCD (mm-2)
600
400
200
0
0
4000
8000
12000
16000
FCSA (µm2)
H
LCFR
4
3
2
1
0
0
4000
8000
12000
16000
FCSA (µm2)
I
LCD (mm-2)
600
400
200
0
0
4000
8000
12000
16000
FCSA (µm2)

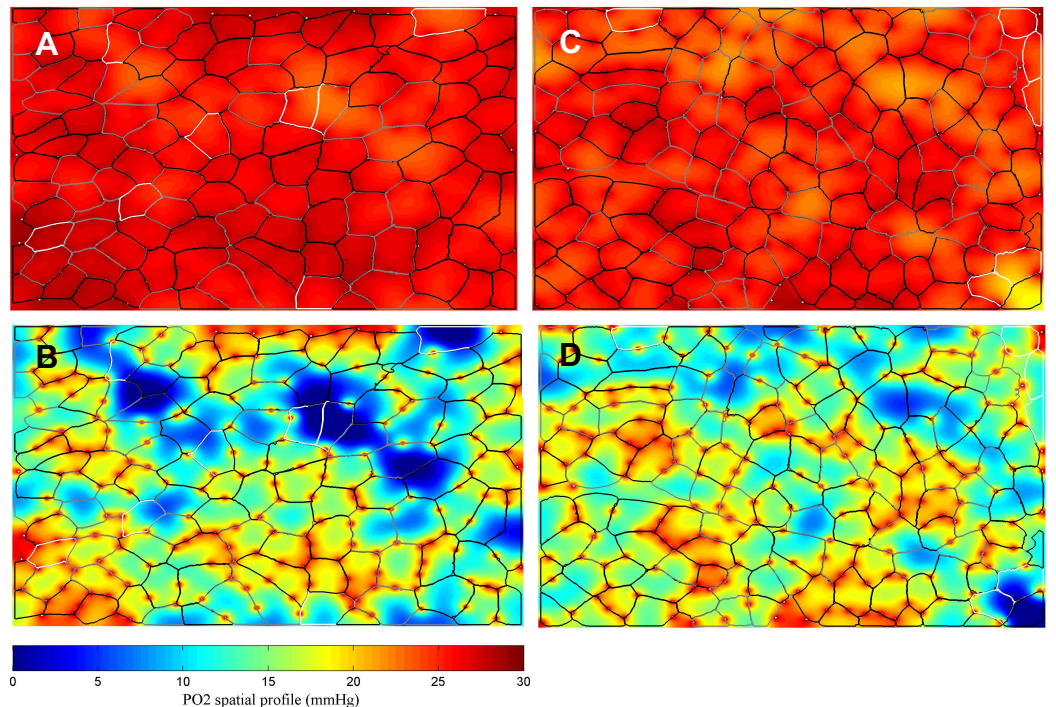
A
C
B
D
0
5
10
15
20
25
30
PO2 spatial profile (mmHg)

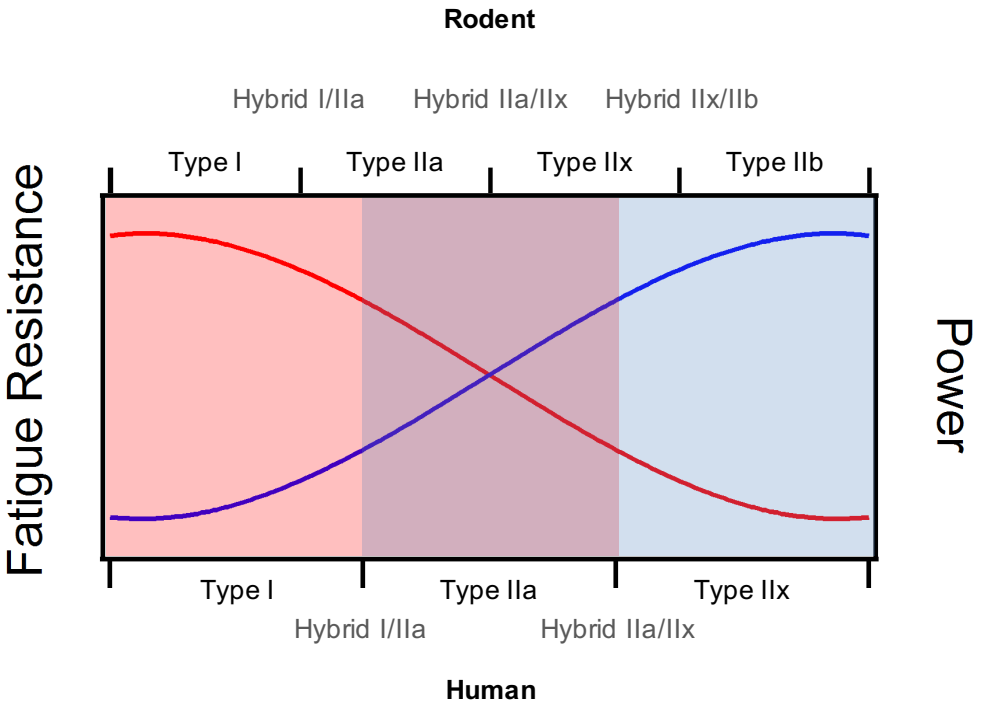
Rodent
Hybrid I/IIa
Hybrid IIa/IIx
Hybrid IIx/IIb
Type I
Type IIa
Type IIx
Type IIb
Fatigue Resistance
Power
Type I
Type IIa
Type IIx
Hybrid I/IIa
Hybrid IIa/IIx
Human

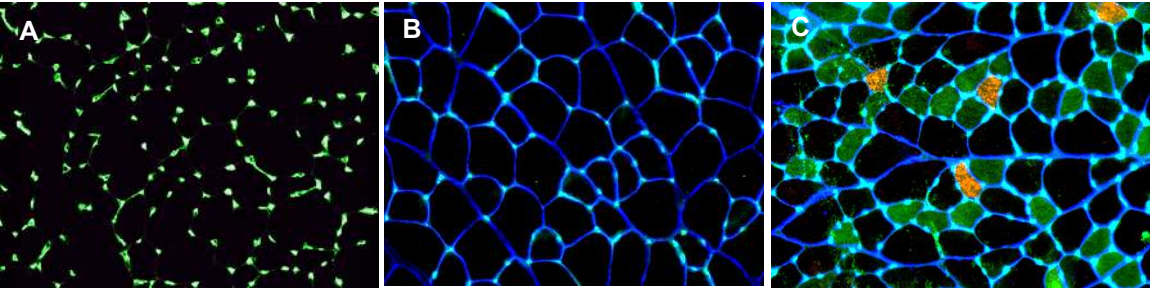
A
B
C